JOURNAL OF AIRCRAFT
Vol. 45, No. 4, July–August 2008

Theoretical and Experimental Aeroelastic Study for Folding Wing Structures

Deman Tang* and Earl H. Dowell†
Duke University, Durham, North Carolina 27708-0300

DOI: 10.2514/1.32754

Folding wing aeroelastic experimental models have been designed and tested in the Duke wind tunnel. The folding wing structure is also modeled theoretically using linear plate theory and divided into three components: the fuselage, the inboard wing, and the outboard wing. A component modal analysis is used to derive the full structural equations of motion for the combined system. A three-dimensional time domain vortex lattice aerodynamic model is used in conjunction with the structural model to investigate the stability of the linear aeroelastic system. The effects of the inboard and outboard torsional stiffness at the attachment points between the components and also the folding angle at the interface lines are discussed. The theoretical and experimental results provide new insights into the folding wing aircraft dynamic behavior and a deeper understanding of aeroelastic stability and its potential impact on a folding wing design.

Nomenclature

$[A]$, $[B]$	=	aerodynamic coefficient matrices for the folding wing system
a_i, b_i, c_i	=	generalized coordinates for components A, B, and C, respectively
K_A, K_B	=	torsional stiffnesses at the attachment points between components A and B and components B and C, respectively
$kmm1$	=	total number of vortices on component A and wake in the x direction
$kmm2$	=	total number of vortices on component B and wake in the ξ_B direction
$kmm3$	=	total number of vortices on component C and wake in the ξ_C direction
$km1$, $kn1$	=	number of vortex elements on component A in the x and y directions, respectively
$km2$, $kn2$	=	number of vortex elements on component B in the ξ_B and η_B directions
$km3$, $kn3$	=	number of vortex elements on component C in the ξ_C and η_C directions
m_{Ai}, m_{Bi}, m_{Ci}	=	modal mass for each component
N_A, N_B, N_C	=	number of structural modal functions for each component
Q^Φ, Q^Ψ, Q^Θ	=	generalized aerodynamic force for each component
q, $\dot{q}$	=	state-space vector
t	=	time
U	=	airspeed
U_f	=	critical flutter velocity
w	=	downwash
z_A, z_B, z_C	=	out-of-plane displacement for components A, B, and C, respectively
Γ	=	vortex strength
Δp	=	aerodynamic pressure loading on panel
Θ	=	transverse modal function for component C
θ_B, θ_C	=	folding angles between components A and B and components B and C, respectively
μ_i	=	modal mass for the folding wing system
Π_i	=	eigenmode for the folding wing system
ρ_∞	=	air density
ν_i	=	generalized coordinate of the folding wing system
Φ	=	transverse modal function for component A
Ψ	=	transverse modal function for component B
Ω_i	=	natural frequency for the folding wing system
ω_{Ai}, ω_{Bi}, ω_{Ci}	=	natural frequencies for each component
ω_f	=	flutter frequency for the folding wing system

Received 11 June 2007; revision received 19 February 2008; accepted for publication 19 February 2008.

*Research Scientist, Department of Mechanical Engineering and Materials Science.

†William Holland Hall Professor, Department of Mechanical Engineering and Materials Science and Member of the Center for Nonlinear and Complex Systems; also Dean Emeritus, Pratt School of Engineering. Fellow AIAA.

I. Introduction

RECENT advances in aerospace technologies during the last decade may yield significant changes for future aircraft design. These technologies enable new ways of changing an aircraft's geometry while in-flight. Substantial geometric changes may permit efficient performance during disparate mission roles or allow new multirole missions not possible with a fixed-geometry aircraft. For example, a *morphing* aircraft wing could be capable of substantially changing its shape and size in-flight to enable a single vehicle to perform multiple mission roles. Several research programs and efforts are underway for morphing aircraft. NASA's Aircraft Morphing program [1] and the Defense Advanced Research Projects Agency's Morphing Aircraft Structures program [2] are examples of larger coordinated efforts to develop morphing aircraft. One strong candidate for morphing wing design is a folding wing configuration. Several parametric studies have been performed to identify the aeroelastic characteristics of a generic folding wing configuration [3–7]. These studies show that, as the inboard wing folding angle increases, the flutter dynamic pressure increases. Also, for the fully folding wing configuration, the flutter dynamic pressure is much more sensitive to changes in the outboard hinge stiffness than the inboard hinge stiffness.

Building on previous work (see [3–5]), the objective of this paper is to develop a new and more effective theoretical/computational method for morphing aircraft design and also an experimental model for verification of the computational method to provide an assessment of aeroelastic stability. The parameter studies will include the assessment of the inboard and outboard wing folding angles, the hinge line flexibility, and the sweep angle of the outboard wing. The work includes computationally modeling a set of inboard and outboard wings with different geometric shapes and sweep angles. The structural eigenmodes of the complete wing are then obtained from each component of the wing and fuselage. Using a

component modal technique and a vortex lattice aerodynamic model, the flutter instability of a complete folding wing with varying wing folding angles can be determined when the hinge line stiffness is included in the component mode model. The component mode has the advantage that a parameter change in one component does not require any change in the analysis of other components. The vortex lattice method was chosen because of its simplicity in modeling the aerodynamic flow. The doublet lattice method could also be used but, for the present application, would give results of similar accuracy at a comparable computational cost.

To evaluate the theoretically predicted structural dynamics and flutter characteristics of the folding wing model, an experimental investigation has been carried out in the Duke wind tunnel. In the experimental investigation, both the flutter and limit cycle oscillations (LCOs) were found. However, a theoretical investigation of LCOs was not undertaken, but is left to future investigations. The present theoretical and experimental investigation provides a deeper understanding of aeroelastic stability and its potential impact on the folding wing design.

The motivation for the present work was to conduct an aeroelastic theoretical and experimental study of a representative folding wing configuration. No claim is made regarding the aerodynamic advantages of the chosen configuration relative to any other.

II. Theoretical Basis

A. Structural Motion Equations

A schematic of a folding wing geometry is shown in Fig. 1. The folding wing system consists of three separate components: component A, that is, the fuselage; component B, that is, the inboard wing; and component C, that is, the outboard wing. Components A and B are attached through a hinge that is modeled as a set of torsional springs at several points, P_j. Each torsional spring stiffness is K_{Aj}. Also, components B and C are attached by a hinge that is modeled as a set of torsional springs at several points, S_j. The torsional spring stiffness is K_{Bj}. The hinge model is assumed to have negligible weight compared with the wing structure model. The dynamic effect of the hinge weight was neglected. The initial folding angles between components A and B and components B and C are θ_B and θ_C, respectively. Note that θ_B and θ_C are the static equilibrium angles. These depend upon the initial unsprung wing folding angle and the spring deformation due to wing gravity. Component A is assumed to be a clamped-free plate, and the components B and C are assumed to be free–free plates. In addition to the main coordinate system, xyz, two additional subcoordinate systems, $\zeta_B\eta_B\xi_B$ and $\zeta_C\eta_C\xi_C$ for components B and C, are used as shown in Fig. 1. There are relationships among the main coordinate system and the subcoordinate systems of components A and B. These are expressed as follows:

$$\begin{Bmatrix} x \\ y \\ z \end{Bmatrix}_B = \begin{Bmatrix} l_A \tan\beta_0 \\ l_A \\ 0 \end{Bmatrix} + \begin{bmatrix} 1 & 0 & 0 \\ 0 & \cos\theta_B & -\sin\theta_B \\ 0 & \sin\theta_B & \cos\theta_B \end{bmatrix} \begin{Bmatrix} \zeta \\ \eta \\ \xi \end{Bmatrix}_B \tag{1}$$

$$\begin{Bmatrix} x \\ y \\ z \end{Bmatrix}_C = \begin{Bmatrix} (l_A + l_B\cos\theta_B)\tan\beta_0 \\ l_A + l_B\cos\theta_B \\ l_B\sin\theta_B \end{Bmatrix} + \begin{bmatrix} 1 & 0 & 0 \\ 0 & \cos\theta_C & -\sin\theta_C \\ 0 & \sin\theta_C & \cos\theta_C \end{bmatrix} \begin{Bmatrix} \zeta \\ \eta \\ \xi \end{Bmatrix}_C \tag{2}$$

The classical Rayleigh–Ritz approach is used for each component. In this approach, each of the out-of-plane displacement variables, z_A, z_B, and z_C, which are a function of x, y, and t, or ζ_B, η_B, and t, or ζ_C, η_C, and t, are expanded in a series of the product of time-dependent modal coordinates and space-dependent functions. One expands the transverse displacement z_A, z_B, and z_C as follows:

$$\begin{cases} z(x,y,t) = \sum_i \Phi_i(x,y)a_i(t), & i = 1\cdots N_A \\ z(\zeta_B,\eta_B,t) = \sum_i \Psi_i(\zeta_B,\eta_B)b_i(t), & i = 1\cdots N_B \\ z(\zeta_C,\eta_C,t) = \sum_i \Theta_i(\zeta_C,\eta_C)c_i(t), & i = 1\cdots N_C \end{cases} \tag{3}$$

where $\Phi_i(x,y)$ is the transverse natural mode function for the clamped-free plate of component A. $\Psi_i(\zeta_B,\eta_B)$ and $\Theta_i(\zeta_C,\eta_C)$ are the transverse natural mode functions for the free–free plate of components B and C. These natural mode functions are calculated using a finite element method (FEM). All such calculations are done using a standard computational FEM code, ANSYS. These functions satisfy the boundary conditions for all of the components. a_i, b_i, and c_i are the generalized coordinates, and N_A, N_B, and N_C are the total number of the generalized coordinates of each component.

For the components B and C, there are three rigid transverse modes and three rigid rotational modes. Both the six rigid body mode shapes and the elastic mode shapes are obtained from the ANSYS code.

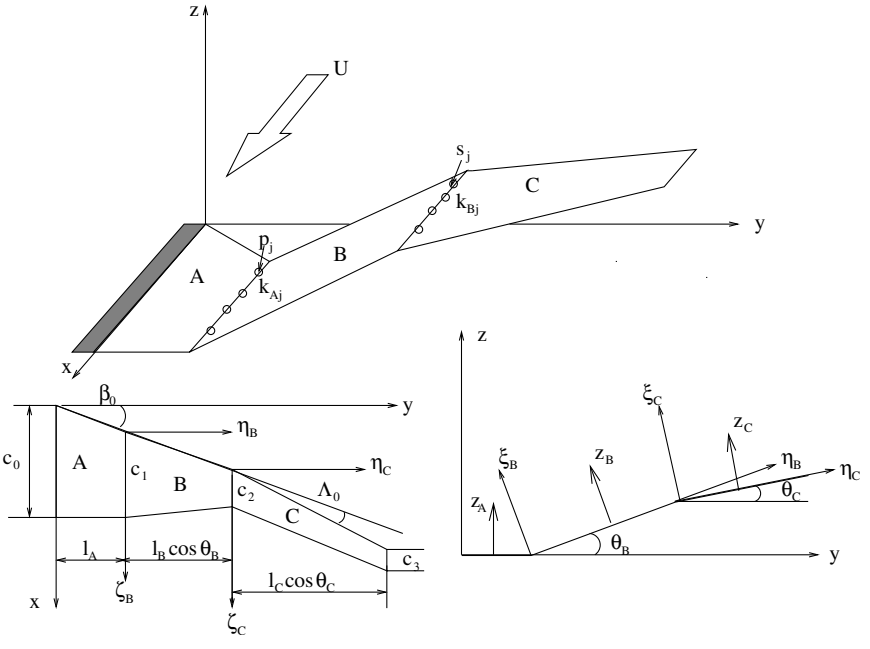

Fig. 1 Schematic of a folding wing geometry and coordinate systems.

The kinetic energy for each component can be written as follows:

$$\begin{cases} T_A = \frac{1}{2}\sum_i m_{Ai}\dot{a}_i^2, & i = 1 \cdots N_A \\ T_B = \frac{1}{2}\sum_i m_{Bi}\dot{b}_i^2, & i = 1 \cdots N_B \\ T_C = \frac{1}{2}\sum_i m_{Ci}\dot{c}_i^2, & i = 1 \cdots N_C \end{cases}$$

The total kinetic energy is

$$T = T_A + T_B + T_C = \tfrac{1}{2}\lfloor \dot{q} \rfloor [M_{qq}]\{\dot{q}\} \tag{4}$$

where

$$\{q_i\} = \{a_i, b_i, c_i\}^T$$

and $[M_{qq}]$ is a diagonal modal mass matrix and m_{Ai}, m_{Bi}, and m_{Ci} are the modal mass for each component. The modal mass for both the rigid and elastic modes is defined as a unit (kg) by the ANSYS code.

The potential energy for each component is expressed as

$$\begin{cases} V_A = \frac{1}{2}\sum_i \omega_{Ai}^2 a_i^2, & i = 1 \cdots N_A \\ V_B = \frac{1}{2}\sum_i \omega_{Bi}^2 b_i^2, & i = 1 \cdots N_B \\ V_C = \frac{1}{2}\sum_i \omega_{Ci}^2 c_i^2, & i = 1 \cdots N_C \end{cases}$$

where ω_{Ai}, ω_{Bi}, and ω_{Ci} are the ith natural frequencies of each component.

The connections between components A and B and components B and C are elastic hinges with torsional stiffnesses, K_{Aj} and K_{Bj}, at the attachment points, P_j and S_j. The potential energies at the attachment points are

$$\begin{cases} V_{A-B} = \frac{1}{2}\sum_j K_{Aj}\left(\frac{\partial z_A}{\partial y}\big|_{y=l_A} - \frac{\partial z_B}{\partial \eta_B}|\eta_B = 0\right)^2, & j = 1 \cdots N_P \\ V_{B-C} = \frac{1}{2}\sum_j K_{Bj}\left(\frac{\partial z_B}{\partial \eta_B}\big|_{\eta_B=l_B} - \frac{\partial z_C}{\partial \eta_C}\big|_{\eta_C=0}\right)^2, & j = 1 \cdots N_S \end{cases}$$

where N_P and N_S are the total number of the attachment points of the two hinge lines.

The total potential energy is

$$V = V_A + V_B + V_C + V_{A-B} + V_{B-C} = \tfrac{1}{2}\lfloor q \rfloor [K_{qq}]\{q\} \tag{5}$$

where $[K_{qq}]$ is the stiffness matrix.

The generalized nonconservative virtual work for each component can be expressed as

$$\begin{cases} \delta W_A = \sum_i \Delta p_i^A \Delta x_i \Delta y_i \delta z_A(x_i, y_i, t), & i = 1 \cdots M_A \\ \delta W_B = \sum_i \Delta p_i^B \Delta \zeta_{Bi} \Delta \eta_{Bi} \delta z_B(\zeta_{Bi}, \eta_{Bi}, t), & i = 1 \cdots M_B \\ \delta W_C = \sum_i \Delta p_i^C \Delta \zeta_{Ci} \Delta \eta_{Ci} \delta z_C(\zeta_{Ci}, \eta_{Ci}, t), & i = 1 \cdots M_C \end{cases}$$

where Δp_i^A, Δp_i^B, and Δp_i^C are the aerodynamic pressure loadings, and δz_A, δz_B, and δz_C are the virtual translation at the coordinate of the vortex lattice points over each component. M_A, M_B, and M_C are the total number of the vortex elements for each component.

The total virtual work is

$$\delta W = \delta W_A + \delta W_B + \delta W_C \tag{6}$$

The constraint conditions at the attachment points P_j and S_j are

$$\begin{cases} f_{pj} = z_A(P_j) - z_B(P_j)\cos\theta_B = 0, & j = 1 \cdots N_P \\ f_{Sj} = z_B(S_j)\cos\theta_B - z_C(S_j)\cos\theta_C = 0, & j = 1 \cdots N_S \end{cases} \tag{7}$$

The Lagrangian is

$$L = T - V + \sum_{j=1}^{N_P} \lambda_{Pj} f_{Pj} + \sum_{j=1}^{N_S} \lambda_{Sj} f_{Sj} \tag{8}$$

where λ_{Pj} and λ_{Sj} are the Lagrange multipliers. λ (λ_{Pj} or λ_{Sj}) is an arbitrary function of time. Thus, we may choose λ such that the coefficients of the virtual changes in each of the dependent generalized coordinates is zero.

Substituting Eqs. (3–8) into Lagrange's equations gives a system of second-order linear ordinary differential equations:

$$\begin{bmatrix} M_{qq} & 0 \\ 0 & 0 \end{bmatrix} \begin{Bmatrix} \ddot{q} \\ \ddot{\lambda} \end{Bmatrix} + \begin{bmatrix} K_{qq} & K_{q\lambda} \\ K_{\lambda q} & 0 \end{bmatrix} \begin{Bmatrix} q \\ \lambda \end{Bmatrix} = \begin{Bmatrix} Q \\ 0 \end{Bmatrix} \tag{9}$$

When the aerodynamic force vector, $\{Q\}$, is assumed to be zero, one obtains an eigenvalue and the eigenmode matrices of $[\Omega]$ and $[\Pi]$ for the folding wing structure. For details of the structural modal analysis, see Chapter 10 of Dowell and Tang [8].

Based upon the eigenmodes of $[\Omega]$, $[\Pi]$ for the folding wing system, a reconstruction of the structural motion equation may be derived.

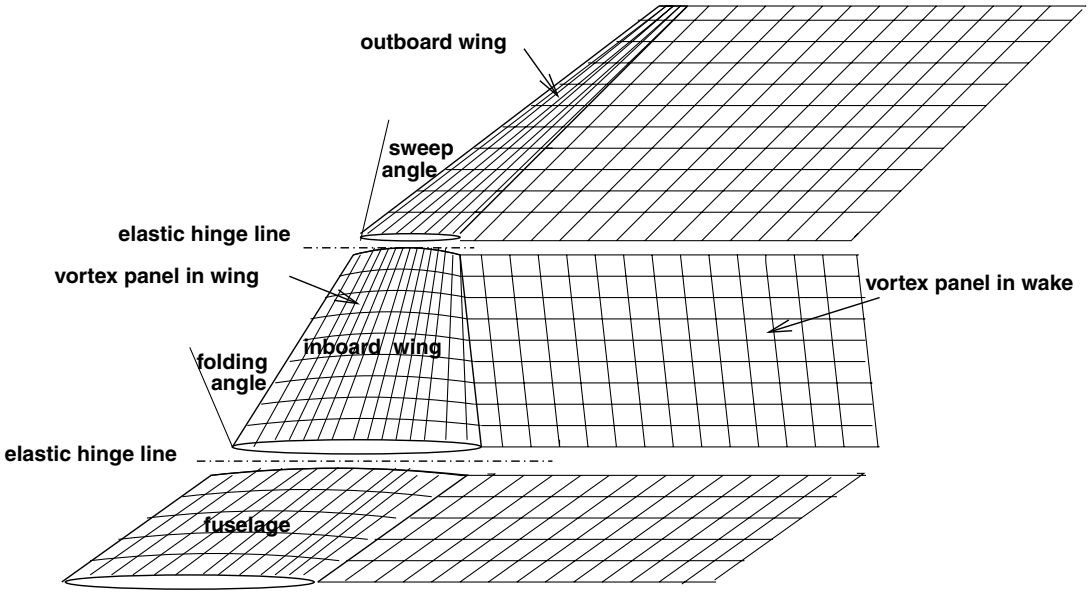

Fig. 2 Schematic of a folding wing structural model with the vortex lattice aerodynamic grid.

Table 1 Natural frequencies vs the outboard folding angles, θ_C, for $\theta_B = 30$ deg and $K_A = K_B = 0.18$ kg m^2/s^2

	$\theta_C = 0$ deg		$\theta_C = 30$ deg		$\theta_C = 60$ deg	
Mode	Theory, Hz	Test, Hz	Theory, Hz	Test, Hz	Theory, Hz	Test, Hz
1	4.33	4.75	4.13	4.25	3.22	4.0
2	16.10	16.0	15.83	17.25	14.50	15.25
3	31.46	32.5	29.78	31.5	22.13	23.5
4	42.86	43.75	43.96	46.25	48.60	47.5
5	76.44	75.2	76.54	73.25	78.32	75.25
6	99.73	89.5	100.82	91.25	107.09	87.5

Consider a transformation from the coordinates, q, to a new set of coordinates, ν, using the eigenmode transformation matrix, $[\Pi]$:

$$\{q\}_{N_{ABC}\times 1} = [\Pi]_{N_{ABC}\times R}\{\nu\}_{R\times 1}$$

where ν is a new set of (modal) coordinates, and $R \ll N_{ABC}$.

Substituting this equation into the kinetic and potential energy equations, Eqs. (4) and (5), and using Lagrange's equations without the constraint conditions at the attached points, P_j and S_j, gives a final structural modal equation with a modal damping rate, ξ_i:

$$[\mu_i]\{\ddot{\nu}\} + [2\Omega_i\xi_i\mu_i]\{\dot{\nu}\} + [\Omega_i^2\mu_i]\{\nu\} = [\Pi]^T\{Q\} \tag{10}$$

where the modal mass matrix $[\mu_i]$ is diagonal due to the orthogonality conditions.

B. Linear Vortex Lattice Aerodynamic Equations

The flow about the folding wing system is assumed to be incompressible, inviscid, and irrotational. Here we use an unsteady vortex lattice method to model this flow. A schematic of the folding wing geometry with a three-dimensional vortex lattice aerodynamic model including a numerical grid for each component is shown in Fig. 2.

The folding wing and wake are divided into a number of elements. In the wake and on the folding wing, all of the elements are of equal size, Δx, in the streamwise direction. Point vortices are placed on the folding wing and in the wake at the quarter chord of the elements. At the three-quarter chord of each element, a collocation point is placed for the downwash, that is, the velocity induced by the discrete vortices is set as equal to the downwash arising from the unsteady motion of the folding wing. Thus, we have the relationship

$$w_i^{t+1} = \sum_j K_{ij}\Gamma_j^{t+1}, \qquad i = 1\cdots M_{ABC} \tag{11}$$

where w_i^{t+1} is the downwash at the ith collocation point at time step $t+1$, Γ_j is the strength of the jth vortex, and K_{ij} is an aerodynamic kernel function. M_{ABC} is the number of total collocation points on the folding wing.

An aerodynamic matrix equation is then formed:

$$[A]\{\Gamma\}^{t+1} + [B]\{\Gamma\}^t = [T]\{w\}^{t+1} \tag{12}$$

where $[A]$ and $[B]$ are aerodynamic coefficient matrices that depend upon the kernel function of the horseshoe vortex in space and the wake vortex for the folding wing system. (For a detailed derivation of the kernel function, see [9,10].) $[T]$ is a transfer matrix for determining the relationship between the global vortex lattice mesh and the local vortex lattice mesh on the folding wing system.

The downwash at the ith collocation point of the folding wing arising from the unsteady motion of the folding wing can be expressed in a matrix form as

$$[T]\{w\}^{t+1} = [T]\left(\begin{Bmatrix}\dot{z}_A\\ \dot{z}_B\\ \dot{z}_C\end{Bmatrix} + U_\infty\begin{Bmatrix}\partial z_A/\partial x\\ \partial z_B/\partial x\\ \partial z_C/\partial x\end{Bmatrix}\right) = [E]\{\nu\}^{t+1} \tag{13}$$

where matrices $[E]$ depend upon the eigenmodes $[\Phi]$, $[\Psi]$, and $[\Theta]$ of each component and the modal shape of $[\Pi]$ for the new coordinate system.

Thus, the aerodynamic equation becomes

$$[A]\{\Gamma\}^{t+1} + [B]\{\Gamma\}^t = [E]\{\nu\}^{t+1} \tag{14}$$

C. Aeroelastic State-Space Equations

From the fundamental aerodynamic theory, we can obtain the pressure distribution on the plate at the jth point in terms of the vortex strengths. The aerodynamic pressure is given by

$$\Delta p_j = \frac{\rho_\infty}{\Delta x}\left[U(\Gamma_j^{t+1} + \Gamma_j^t)/2 + \sum_i^j \Delta x(\Gamma_i^{t+1} - \Gamma_i^t)/\Delta t\right] \tag{15}$$

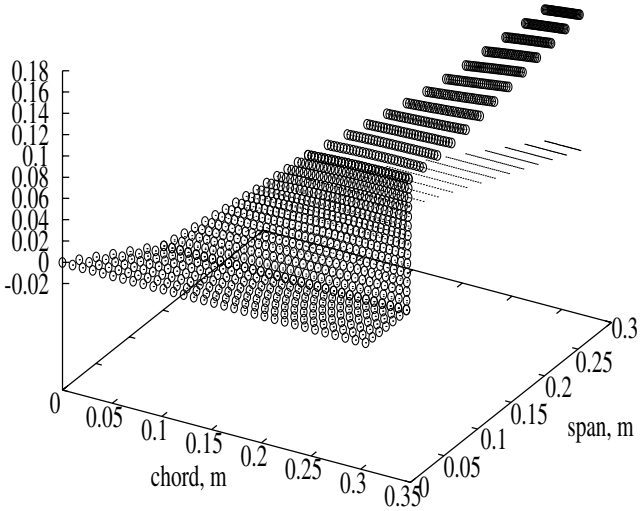

Fig. 3 The first mode shape of the folding wing model for $\Omega_1 = 4.33$ Hz, $K_A = K_B = 0.18$ kg m^2/s^2, $\theta_B = 30$ deg, and $\theta_C = 0$ deg.

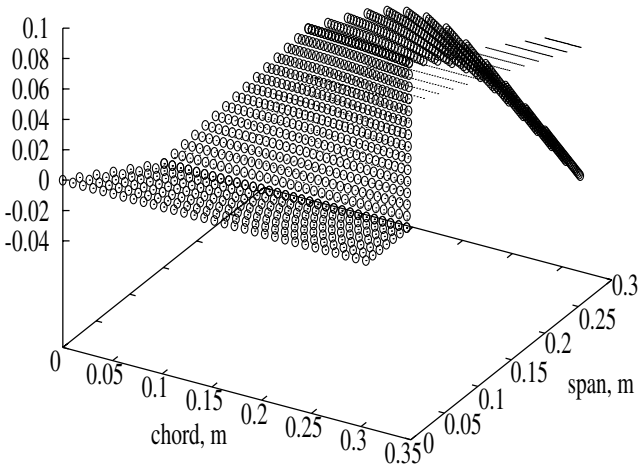

Fig. 4 The second mode shape of the folding wing model for $\Omega_2 = 16.08$ Hz, $K_A = K_B = 0.18$ kg m^2/s^2, $\theta_B = 30$ deg, and $\theta_C = 0$ deg.

and the aerodynamic generalized forces loading on components A, B, and C are calculated from

$$Q_k^{\Phi} = \iint \Delta p_i \Phi_i^k \, \mathrm{d}x_i \, \mathrm{d}y_i \qquad i = 1 \cdots M_A$$
$$Q_k^{\Psi} = \iint \Delta p_i \Psi_i^k \, \mathrm{d}\zeta_{Bi} \eta_{Bi} \qquad i = 1 \cdots M_B \tag{16}$$
$$Q_k^{\Theta} = \iint \Delta p_i \Theta_i^k \, \mathrm{d}\zeta_{Ci} \eta_{Ci} \qquad i = 1 \cdots M_C$$

where M_A, M_B, and M_C are the total number of aerodynamic element panels of each component.

$$\{Q\}_{N_{ABC}\times 1} = \begin{Bmatrix} Q^{\Phi} \\ Q^{\Psi} \\ Q^{\Theta} \end{Bmatrix} = [\mathcal{B}]_{N_{ABC}\times M_{ABC}} \{\Delta p\}_{M_{ABC}\times 1} \tag{17}$$

where $\{\Delta p\}$ is the aerodynamic pressure difference at the vortex point over the complete folding wing and $[\mathcal{B}]$ is a combined modal shape matrix corresponding to the vortex points of each component. M_{ABC} is the total number of total aerodynamic panel elements (or total collocation points) of the folding wing, $M_{ABC} = M_A + M_B + M_C$.

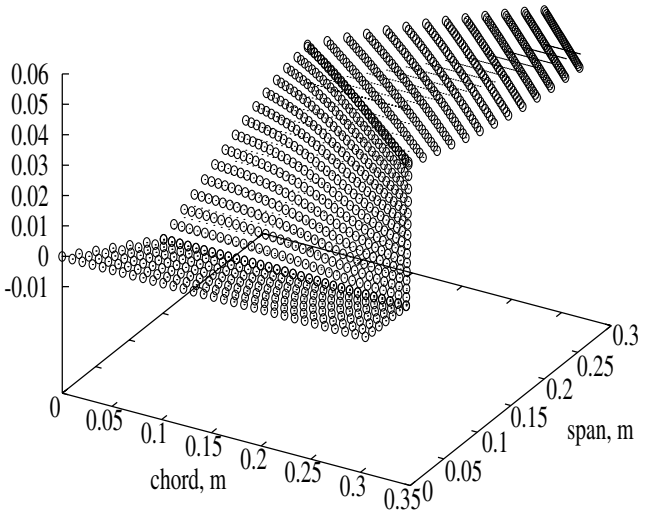

Fig. 5 The third mode shape of the folding wing model for $\Omega_3 = 31.46$ Hz, $K_A = K_B = 0.18$ kg m^2/s^2, $\theta_B = 30$ deg, and $\theta_C = 0$ deg.

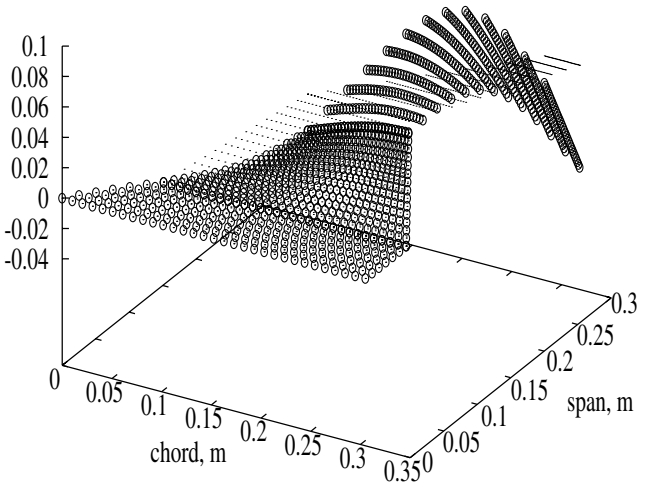

Fig. 6 The fourth mode shape of the folding wing model for $\Omega_4 = 42.82$ Hz, $K_A = K_B = 0.18$ kg m^2/s^2, $\theta_B = 30$ deg, and $\theta_C = 0$ deg.

Substituting Eq. (15) into Eq. (17), and premultiplying Eq. (17) by $[\Pi]^T$ gives

$$[\Pi]^T\{Q\} = [\mathcal{B}_2]\{\Gamma\}^{t+1} + [\mathcal{B}_1]\{\Gamma\}^t \tag{18}$$

where the matrices $[\mathcal{B}_1]$ and $[\mathcal{B}_2]$ depend upon both the eigenmodes of each component and the new modal coordinate system.

Substituting Eq. (18) into Eq. (10), the structural dynamic equations can be reconstituted as a state-space equation in discrete time form as

$$[D_2]\{\theta\}^{t+1} + [D_1]\{\theta\}^t + [C_2]\{\Gamma\}^{t+1} + [C_1]\{\Gamma\}^t = 0 \tag{19}$$

where the vector $\{\theta\}$ is the state of the new modal coordinate system, $\{\theta\} = \{\dot{v}, v\}$, and the matrices $[C_1]$, $[C_2]$, $[D_1]$, and $[D_2]$ only depend upon the structural modal parameters and flow velocity.

Thus, combining Eqs. (14) and (19), we obtain a complete aeroelastic state-space equation in matrix form:

$$\begin{bmatrix} A & -E \\ C_2 & D_2 \end{bmatrix} \begin{Bmatrix} \Gamma \\ \theta \end{Bmatrix}^{t+1} + \begin{bmatrix} B & 0 \\ C_1 & D_1 \end{bmatrix} \begin{Bmatrix} \Gamma \\ \theta \end{Bmatrix}^{t} = \begin{Bmatrix} 0 \\ 0 \end{Bmatrix} \tag{20}$$

Using this equation, the stability of the system (flutter) can be determined.

III. Numerical Results

The theoretical and experimental model is a simple folding wing configuration. The fuselage (component A) is modeled by a uniform plastic (Lucite) plate with a 2.38-mm thickness. The root chord is clamped (cantilevered), and the length of the root chord is 30.48 cm. The inboard wing is modeled by an aluminum plate with a 0.254-mm thickness with several different folding angles, θ_B. There are five

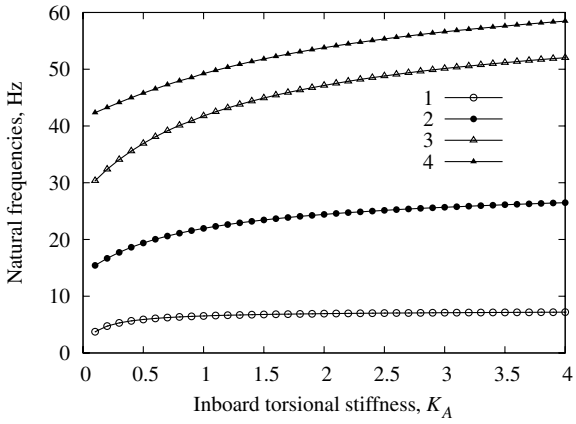

a) K_A varies and $K_B = 0.18$ kgm^2/s^2

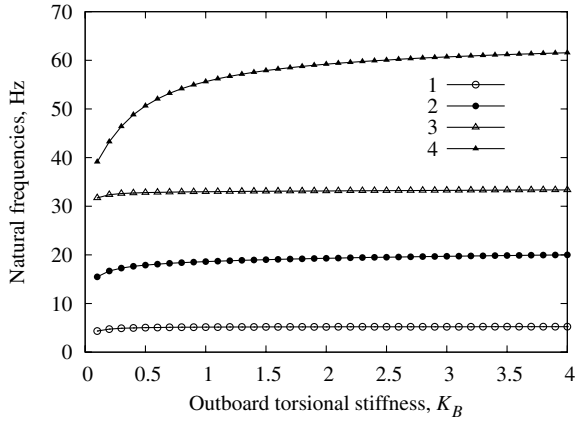

b) K_B varies and $K_A = 0.18$ kgm^2/s^2

Fig. 7 First four natural frequencies vs torsional stiffness at the attachment points for $\theta_B = 30$ deg and $\theta_C = 0$ deg.

attachment points to connect component A and B at 0.81, 6.5, 12.2, 17.8, and 23.6 cm along the chord. At each attachment point, the torsional stiffness of the elastic hinges is assumed to be equal, K_A. The outboard wing is modeled by a similar aluminum plate with a 0.254-mm thickness and several different folding angles, θ_C. There are three attachment points to connect components B and C at 1.0, 5.8, and 9.14 cm along the chord. At each attachment point, the torsional stiffness of the elastic hinges is assumed to be equal, K_B. The mesh of the finite element model for the out-of-plane structural model is 30×30 and, thus, each component wing is modeled using 900 quadrilateral plate elements. The nodes at the root chord for component A satisfy clamped geometric boundary conditions, that is, $w = u = v = \theta_x = \theta_y = \theta_z = 0$. But the nodes at the edges of the plate for components B and C satisfy free–free geometric boundary conditions and, thus, have six rigid body modes.

A linear aerodynamic vortex lattice model is used with vortex elements on each component and correspondingly in the wake. For component A, there are 84 vortex elements ($km1 = 30$, $kn1 = 3$) and 180 vortex elements in the wake ($kmm1 = 90$). For component B, there are 126 vortex elements ($km2 = 24$, $kn2 = 7$) and 336 vortex elements in the wake ($kmm1 = 72$). For component C, there are 45 vortex elements ($km3 = 10$, $kn3 = 6$) and 180 vortex elements in the wake ($kmm1 = 40$). The total number of vortex elements for the folding wing are 951.

A. Results for Structural Dynamic Modes

In the following calculation, we consider each structural component using the ANSYS code and calculate the natural frequencies and corresponding natural modes of the folding wing structure using a component modal analysis as presented in this paper. Only the first 10 elastic eigenmodes and the rigid body modes of components B and C are taken into account in the calculations. The basic parameters are the torsional stiffness, $K_A = K_B = 0.18\ \text{kg m}^2/\text{s}^2$,; the inboard folding angle, $\theta_B = 30$ deg; and the outboard folding angle, $\theta_C = 0$ deg.

The corresponding first six natural frequencies of the total folding wing model from the component mode analysis are shown in Table 1. The first four mode shapes are shown in Figs. 3–6 by the circled dot symbol. For reference, the undeflection folding wing coordinate is also shown in these figures by the dot symbol. The first mode is dominated by the first bending mode of component C. The second mode is dominated by the second bending mode of component C. The third mode is dominated by the first torsion of component C and the first bending mode of component B. The fourth mode is dominated by the first torsion of component B and the second bending mode of component C.

1. *Effect of Torsional Stiffness at Attachment Points*

The effects of the torsional stiffness, K_A and K_B, on the natural frequencies of the folding wing model are considered next. The nominal inboard folding angle is $\theta_B = 30$ deg and the outboard folding angle is $\theta_C = 0$ deg. When the outboard torsional stiffness is set to $K_B = 0.18\ \text{kg m}^2/\text{s}^2$ and the inboard torsional stiffness, K_A, varies from 0.05 to 4 $\text{kg m}^2/\text{s}^2$, the first four natural frequencies are shown in Fig. 7a. When the inboard torsional stiffness is set to $K_A = 0.18\ \text{kg m}^2/\text{s}^2$ and the outboard torsional stiffness, K_B, varies from 0.05 to 4 $\text{kg m}^2/\text{s}^2$, the first four natural frequencies are shown in Fig. 7b. As expected, the effects are significant but, when the torsional stiffness is larger than 2.5 $\text{kg m}^2/\text{s}^2$ for K_A and 1.0 $\text{kg m}^2/\text{s}^2$ for K_B, the effects of further increases are small.

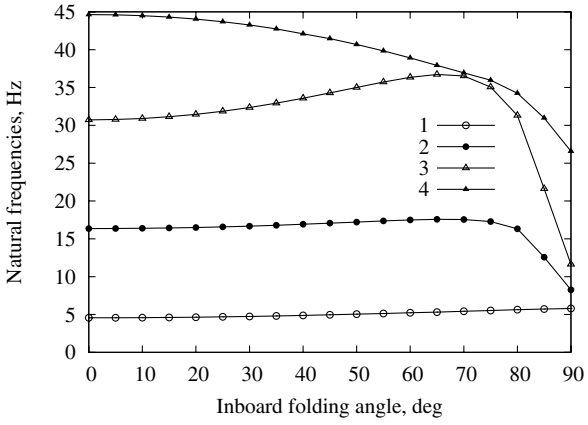

a) θ_B varies and $\theta_C = 0$ deg

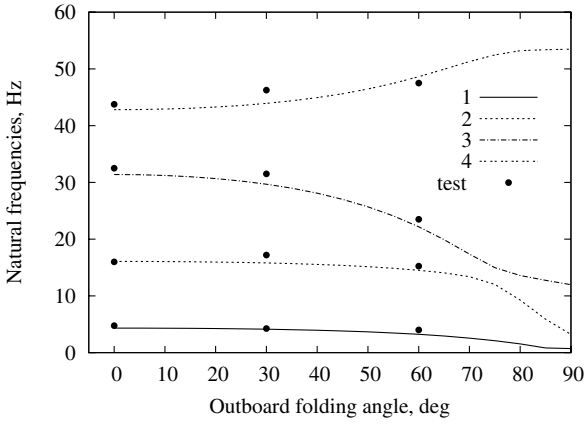

b) θ_C varies and $\theta_B = 30$ deg

Fig. 8 First four natural frequencies vs the folding angle at the attachment points for $K_A = K_B = 0.18\ \text{kg m}^2/\text{s}^2$.

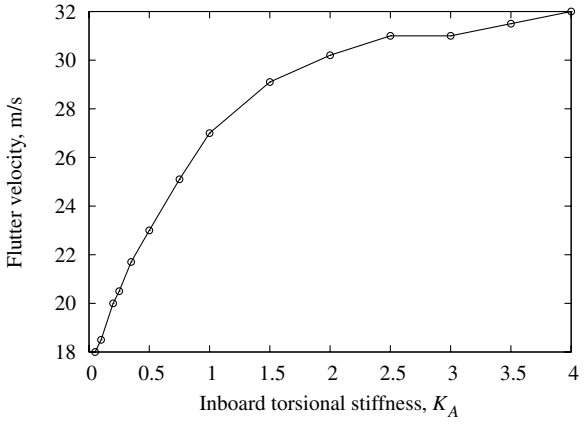

a) Flutter velocity

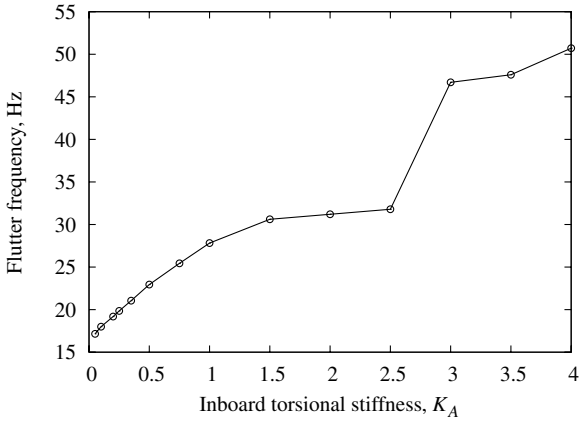

b) Flutter frequency

Fig. 9 Flutter velocity and frequency vs the inboard torsional stiffness, K_A, at attachment points for $\theta_B = 30$ deg, $\theta_C = 0$ deg, and $K_B = 0.18\ \text{kg m}^2/\text{s}^2$.

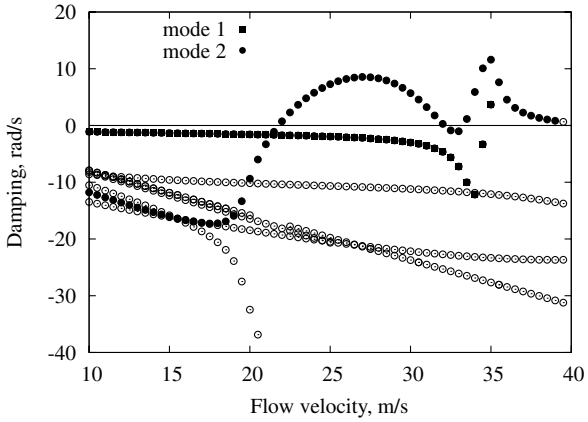

a) Real part

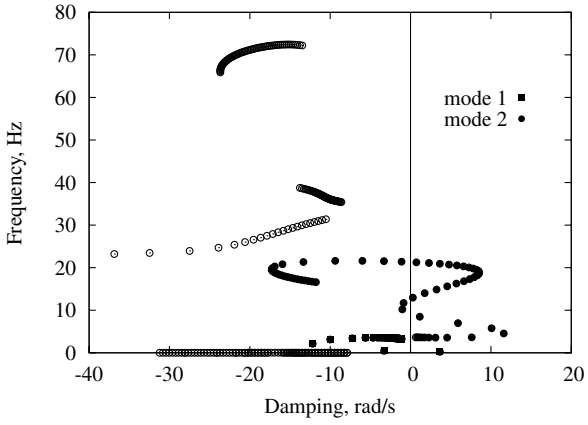

b) Root locus

Fig. 10 Graphical representations of the aeroelastic eigenanalysis for $K_A = 0.35\ \text{kg m}^2/\text{s}^2$, $\theta_B = 30$ deg, $\theta_C = 0$ deg, and $K_B = 0.18\ \text{kg m}^2/\text{s}^2$.

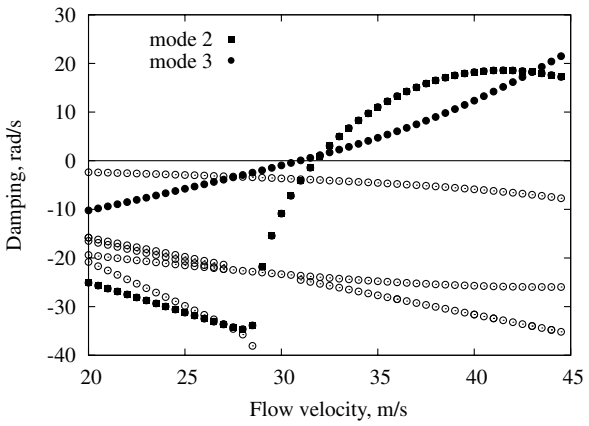

a) Real part

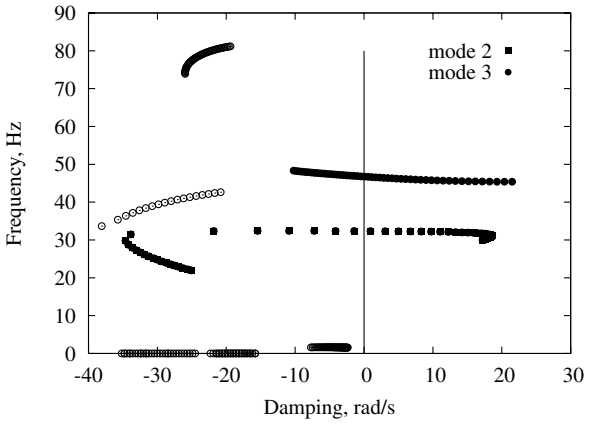

b) Root locus

Fig. 11 Graphical representations of the aeroelastic eigenanalysis for $K_A = 3.0\ \text{kg m}^2/\text{s}^2$, $\theta_B = 30$ deg, $\theta_C = 0$ deg, and $K_B = 0.18\ \text{kg m}^2/\text{s}^2$.

2. Effect of Folding Angle at Interface Line

The effects of the folding angle at the interface line, θ_B and θ_C, on the natural frequencies of the folding wing model are shown in Fig. 8. The nominal inboard and outboard torsional stiffness is $K_A = K_B = 0.18\ \text{kg m}^2/\text{s}^2$. When the outboard folding angle, θ_C, is set to 0 deg and the inboard folding angle, θ_B, varies from 0 to 90 deg, the first four natural frequencies are shown in Fig. 8a. When the inboard folding angle, θ_B, is set to 30 deg and the outboard folding angle, θ_C, varies from 0 to 90 deg, the first four natural frequencies are shown in Fig. 8b. As expected, the effects are also significant.

B. Results for Aeroelastic Stability

The flutter stability of the linearized aeroelastic folding wing model is determined by solving Eq. (20). The aeroelastic eigenvalues obtained from these equations determine the stability of the system. When the real part of any one eigenvalue (damping) becomes positive, the entire system becomes unstable.

1. Effect of Torsional Stiffness on Flutter

The effects of the inboard and outboard torsional stiffnesses, K_A and K_B, on the flutter velocity and frequency of the folding wing model are considered next. The nominal inboard folding angle is $\theta_B = 30$ deg and the outboard folding angle is $\theta_C = 0$ deg. When the outboard torsional stiffness is set to $K_B = 0.18\ \text{kg m}^2/\text{s}^2$ and the inboard torsional stiffness, K_A, varies from 0.05 to 4 $\text{kg m}^2/\text{s}^2$, the results are shown in Figs. 9a and 9b. Both the flutter velocity and frequency increase as K_A increases when $K_A < 2.5\ \text{kg m}^2/\text{s}^2$. For $K_A > 2.5\ \text{kg m}^2/\text{s}^2$ the flutter frequency jumps to a higher frequency flutter mode. The flutter velocity remains relatively constant for further increases of K_A for the range shown.

For a more detailed explanation of Fig. 9, the graphical representations of the eigenanalysis in the form of 1) the real (damping) of the eigenvalues vs flow velocity and 2) a root-locus plot for $K_A = 0.35\ \text{kg m}^2/\text{s}^2$ are shown in Figs. 10a and 10b. There are two types of flutter modes. For the primary flutter mode, there are two intersections with the velocity axis at $U_f = 22$ and 31.7 m/s, and the corresponding flutter oscillatory frequencies are $\omega_f = 21.05$ and 13.5 Hz. For the secondary flutter mode, there is an intersection with the velocity axis at $U_f = 32.5$ m/s, and the corresponding flutter oscillatory frequency is $\omega_f = 9.8$ Hz. This former flutter mode is called a "hump"-type flutter. The critical flutter velocity and frequency of this folding wing model are 22 m/s and 21.05 Hz. When the flow velocity is larger than 35 m/s, the folding wing is statically divergent. The frequency is zero, as shown Fig. 10b. It is found that the primary flutter mode is dominated by the coupling between the second and third structural modes and that the secondary flutter mode is dominated by the coupling between the first and second modes (see Figs. 7a and 10b).

The graphical representations of the eigenanalysis in the form of 1) the real (damping) of the eigenvalues vs flow velocity and 2) a root-locus plot for $K_A = 3.0\ \text{kg m}^2/\text{s}^2$ are shown in Figs. 11a and 11b. There are two flutter velocities, 31 and 32 m/s, and the corresponding oscillatory frequencies are 46.7 and 31.8 Hz. The primary flutter mode is dominated by the coupling between the third structural and fourth modes, and the secondary flutter mode is dominated by the coupling between the second and third modes. The critical flutter velocity and frequency of this folding wing model are 31 m/s and 46.7 Hz.

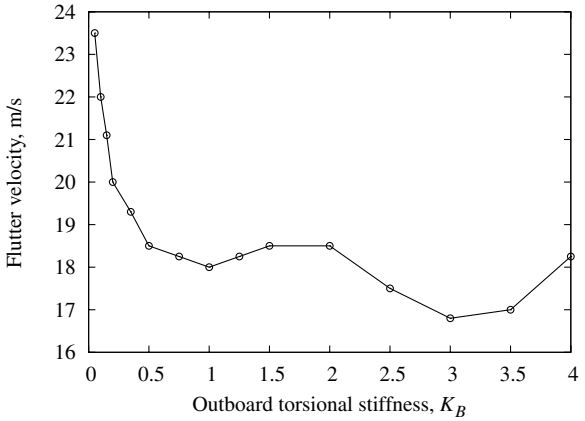

a) Flutter velocity

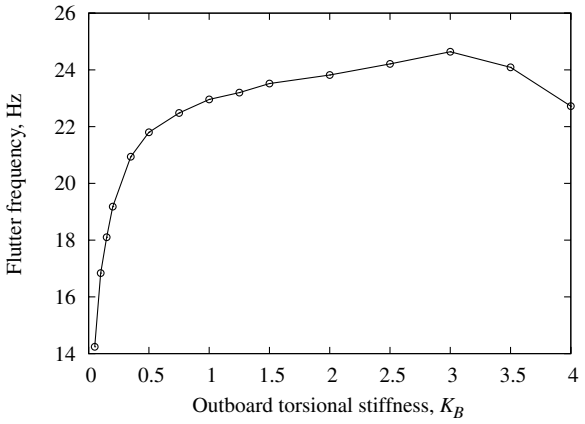

b) Flutter frequency

Fig. 12 Flutter velocity and frequency vs the outboard torsional stiffness, K_B, at the attachment points for $\theta_B = 30$ deg, $\theta_C = 0$ deg, and $K_A = 0.18$ kg m^2/s^2.

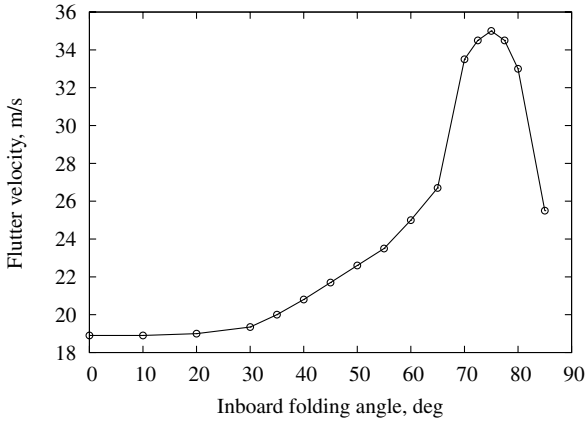

a) Flutter velocity

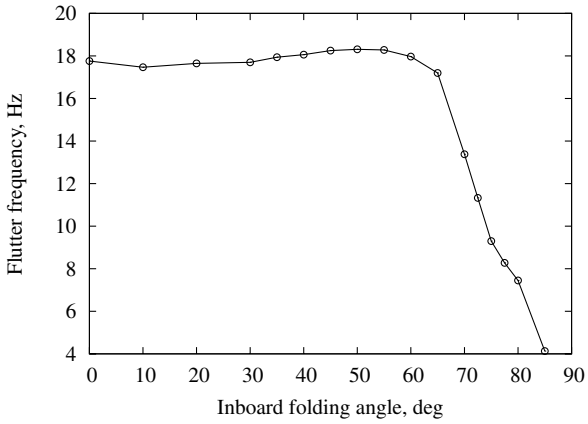

b) Flutter frequency

Fig. 13 Flutter velocity and frequency vs the inboard folding angle, θ_B, at the attachment points for $\theta_C = 0$ deg and $K_A = 0.18$ kg m^2/s^2.

When the inboard torsional stiffness is set to $K_A = 0.18$ kg m^2/s^2 and the outboard torsional stiffness, K_B, varies from 0.05 to 4 kg m^2/s^2, the results are shown in Figs. 12a and 12b. The flutter velocity decreases and the flutter frequency increases as K_B increases. Recalling Fig. 7b, the effects of the torsional stiffness on the flutter behavior should be significant when K_B is less than 0.5 kg m^2/s^2 because of the significant natural frequency variation. However, the effects of further increases are expected to be small.

As expected, the effects of both the inboard and outboard torsional stiffnesses on the flutter behavior are significant.

2. Effect of Folding Angle

The effects of the folding angles at the interface line, θ_B and θ_C, on the flutter velocity and frequency of the folding wing model are shown in Figs. 13–15. The inboard and outboard torsional stiffness is $K_A = K_B = 0.18$ kg m^2/s^2. When the outboard folding angle, θ_C, is set to 0 deg and the inboard folding angle, θ_B, varies from 0 to 85 deg, the flutter results are shown in Fig. 13. When $\theta_B < 65$ deg, the flutter velocity increases as θ_B increases but the change in frequency remains small. There is a special condition near $\theta_B = 70$ deg. The flutter velocity jumps to a higher value when θ_B increases from 65 to 70 deg, but the flutter frequency drops to a lower value. Figures 8b and 14b can be used to explain this phenomenon. The flutter mode jumps to a coupling between the first and second modes from a coupling between the second and third modes.

Figure 14 shows the graphical representations of the eigenanalysis in the form of 1) the real (damping) part of the eigenvalues vs the flow velocity and 2) a root-locus plot for $\theta_B = 70$ deg. From these figures, we find two types of flutter modes. One is a primary flutter mode. The flutter velocity and frequency are 33.5 m/s and 13.38 Hz. The primary flutter mode is dominated by coupling between the first and second modes. The secondary flutter mode is dominated by the coupling between the third and fourth modes. The flutter velocity and frequency are 38 m/s and 55 Hz.

When the inboard folding angle, θ_B, is set to 30 deg and the outboard folding angle, θ_C, varies from 0 to 85 deg, the results are shown in Figs. 15a and 15b. Both the flutter velocity and frequency decrease when the outboard folding angle, $|\theta_C|$, increases up to 70 deg. Also, there is a special condition near $\theta_C = 70$ deg. The flutter velocity jumps to a higher value when θ_C increases from 70 to 72 deg, but the flutter frequency drops to a lower value. This is because the flutter mode jumps to a coupling between the first and second modes from a coupling between the second and third modes.

As expected, the effects of the folding angle on the flutter behavior are significant.

IV. Theoretical and Experimental Correlations

The experimental folding wing configuration parameters are the same as for the theoretical model. At each attachment point connecting components A and B and components B and C, the torsional stiffness of the elastic hinges is equal and $K_A = K_B = 0.18$ kg m^2/s^2. Three special outboard folding angles are considered, that is, $\theta_C = 0$, 30, and 60 deg. The inboard folding angle is chosen to be a generic value, $\theta_B = 30$ deg.

A. Correlation for Structural Dynamic Modes

To check the folding wing structural dynamic behavior, vibration tests for three experimental models are made. For the vibration test, a B&K 8200 force transducer fixed near the wing root is randomly excited by a B&K 4810 minishaker and a B&K 2706 power

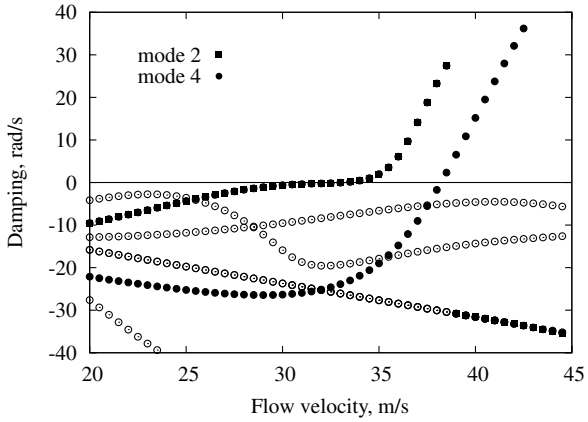

a) Real part

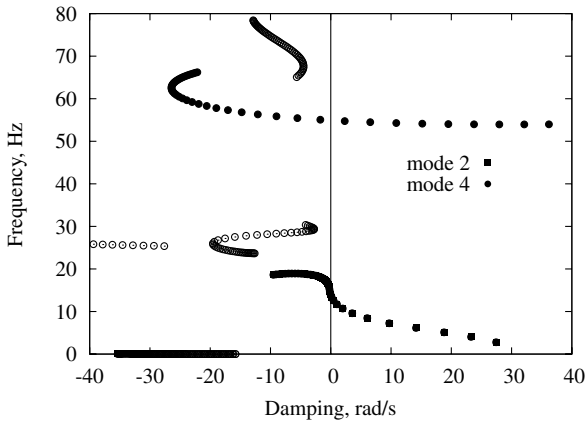

b) Root locus

Fig. 14 Graphical representations of the aeroelastic eigenanalysis for $\theta_B = 70$ deg, $\theta_C = 0$ deg, and $K_A = K_B = 0.18$ kg m^2/s^2.

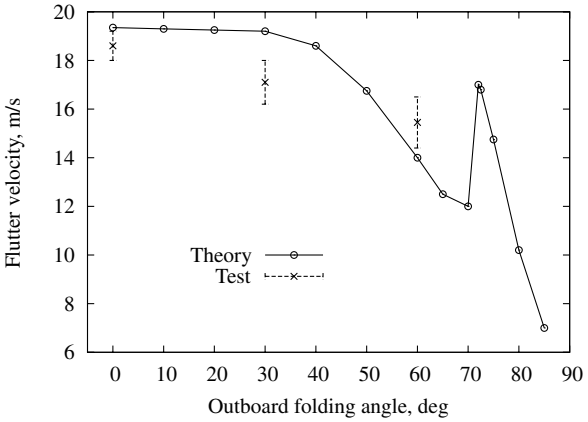

a) Flutter velocity

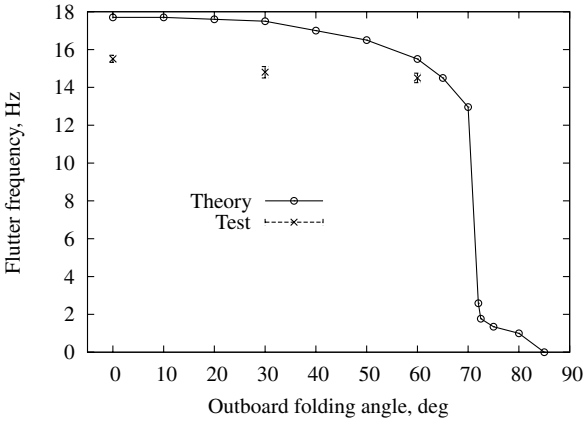

b) Flutter frequency

Fig. 15 Flutter velocity and frequency vs the outboard folding angle, θ_C, at attachment points for $\theta_B = 30$ deg and $K_A = K_B = 0.18$ kg m^2/s^2.

amplifier. The output signal is from a microaccelerometer. A PULSE 3560 four-channel multi-analyzer system is used to measure the autospectrum and coherence between the input force and output acceleration. The experimental setup for the vibration test for the three folding wing models is shown in Figs. 16a–16c, in which $\theta_C = 0$, 30, and 60 deg, respectively. A typical autospectrum and corresponding coherence for $\theta_C = 0$ deg is shown in Fig. 17. The coherence is almost 1 at each resonance frequency and has a lower value at each antiresonance frequency. For the three folding wing structural models, the theoretical and experimental first six natural frequencies are shown in Table 1 and the correlation for the first four natural frequencies are shown in Fig. 8b. The agreement for the natural frequencies is reasonably good, except for $\theta_C = 60$ deg, where the difference for the first mode is about 20%.

B. Correlation for Aeroelastic Stability

For the correlation study of the aeroelastic model, three folding wing configuration models are tested, that is, the outboard folding angle is $\theta_C = 0$, 30, and 60 deg and the inboard folding angle is $\theta_B = 30$ deg. The root of the folding wing model is mounted vertically to a very heavy support frame, which is attached to the ground. A photograph of the experimental folding wing model in the wind tunnel is shown in Fig. 18.

An Ometron VPI 4000 scanning laser vibrometer system is used to measure the velocity deflection at the tip span of the inboard wing trailing edge. The VPI sensor is a noncontacting transducer that uses optical interferometry and electronic frequency measurements to determine the frequency shift of a beam of light reflected from a moving surface.

The velocity responses vs the flow velocity are measured for the three folding wing configurations. The sampling rate is 256 points/s, $\Delta t = 1/256$, and the total sampling length is 2560 points. An ensemble averaged fast Fourier transform (FFT) analysis for 100 realizations is used to determine the velocity amplitude and frequency using a time delay average method. The delay time is $2 \times \Delta t$ and the FFT analysis uses 1024 sampling points. Typical measured time histories for $\theta_C = 30$ deg are shown in Figs. 19a–19c for a flow velocity of $U = 17.5$, 19.9, and 22.48 m/s. The corresponding FFT analysis is shown in Fig. 20. From these signals it is found that the response has an LCO behavior with a dominant frequency, although it is not a pure harmonic motion. There are some beat motions and higher harmonic responses in these time histories. The LCO amplitude increases as the flow velocity increases. When $U < 17.5$ m/s, the response signals do not have an obvious LCO behavior and only have a response to the background noise created by the wind-tunnel turbulence. When $U < 17.5$ m/s, as shown in Fig. 19a, an LCO with a small amplitude occurs. In the present theoretical analysis, we assume that the structure and aerodynamics are linear. No LCO is predicted. But in the present experiment, we did find an LCO, which may be created by either structural or aerodynamic nonlinearities or both.

When the main frequency component is taken from the FFT plot for each flow velocity, the plots of LCO velocity amplitude and LCO frequency vs the flow velocity can be determined. The experimental data have some fluctuation for each FFT analysis due to the turbulent aerodynamic noise. A bar is used in the figure to indicate the magnitude of the measured velocity response uncertainty. The results are shown in Figs. 21a and 21b for the three folding wing configuration models.

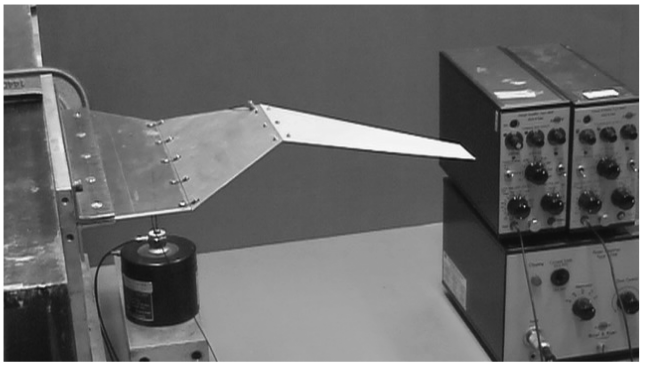

a) $\theta_B = 30^\circ$ and $\theta_C = 0^\circ$

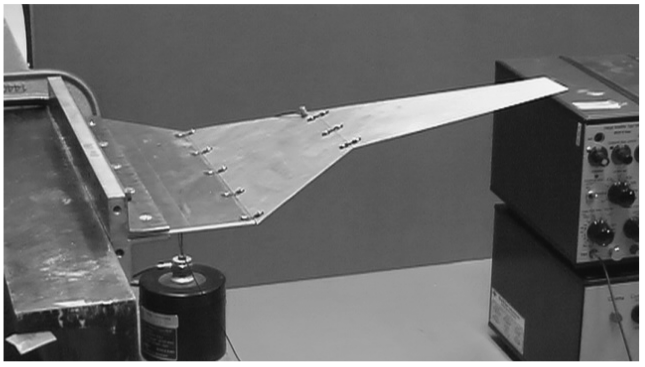

b) $\theta_B = 30^\circ$ and $\theta_C = 30^\circ$

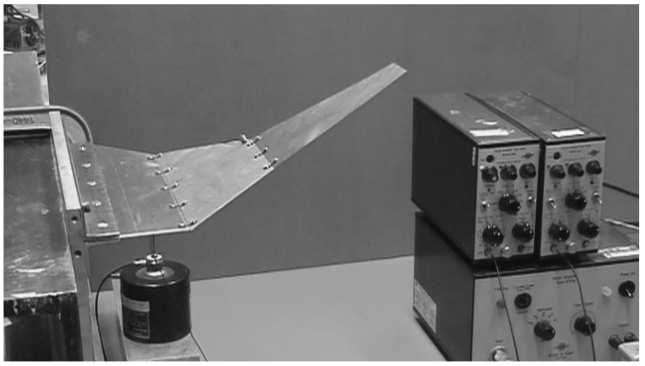

c) $\theta_B = 30^\circ$ and $\theta_C = 60^\circ$

Fig. 16 Vibration test for a folding wing experimental model for an inboard angle of $\theta_B = 30$ deg and outboard angles of $\theta_C = 0$, 30, and 60 deg and $K_A = K_B = 0.18$ kg m^2/s^2.

The linear critical flutter boundary including an error bar can be estimated by using the following method. From Fig. 21, we can determine an upper limit of the linear critical flutter boundary, that is, an intersection between a linear extrapolate of the global LCO amplitude curve (as indicated by a solid line in Fig. 21) and the flow velocity axis. The linear extrapolated line is obtained from the ensemble averaged LCO velocity amplitude. The upper flutter boundary flow velocity is $U_f = 19.2$ m/s and the corresponding frequency is $\omega_f = 15.75$ Hz for $\theta_C = 0$ deg, $U_f = 18.0$ m/s and $\omega_f = 15.1$ Hz for $\theta_C = 30$ deg, and $U_f = 16.5$ m/s and $\omega_f = 14.75$ Hz for $\theta_C = 60$ deg. Also, we can determine a lower limit of the linear critical flutter boundary flow velocity, that is, an intersection between a nonlinear extrapolate of the local LCO amplitude curve near the lower LCO amplitude and the flow velocity axis. The nonlinear extrapolate line is also obtained from the ensemble averaged LCO velocity amplitude. The lower flutter boundary flow velocity is $U_f = 18$ m/s and the corresponding flutter frequency $\omega_f = 15.32$ Hz for $\theta_C = 0$ deg, $U_f = 16.2$ m/s and $\omega_f = 14.5$ Hz for $\theta_C = 30$ deg, and $U_f = 14.4$ m/s and $\omega_f = 14.25$ Hz for $\theta_C = 60$ deg.

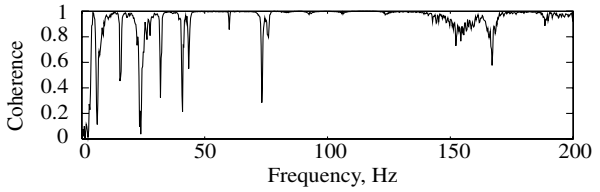

a) Coherence

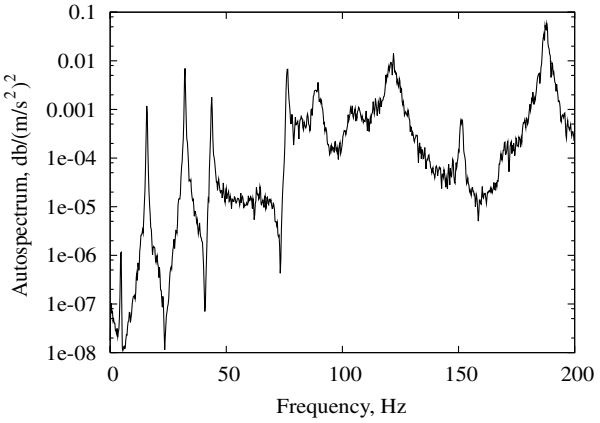

b) Autospectrum

Fig. 17 Coherence and autospectrum response to random excitation for the experimental model, $\theta_B = 30$ deg, $\theta_C = 0$ deg, and $K_A = K_B = 0.18$ kg m^2/s^2.

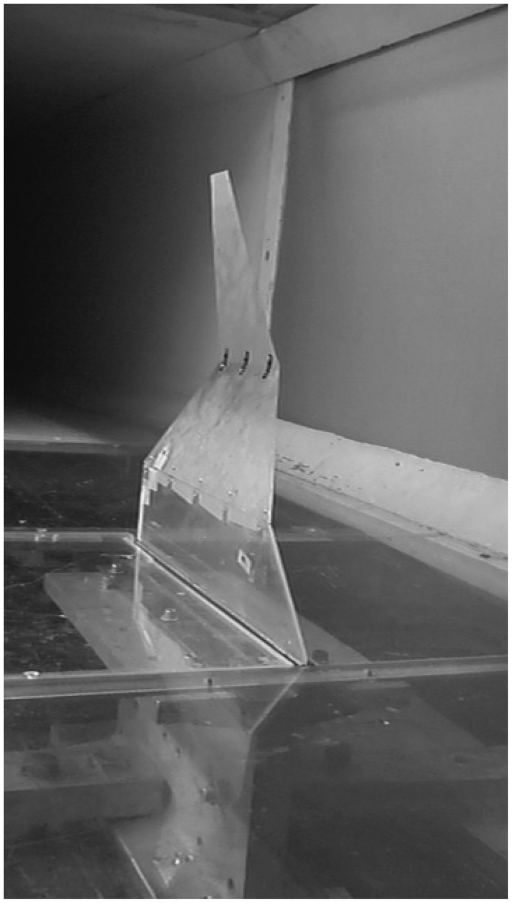

Fig. 18 Photograph of the experimental folding wing model for $\theta_C = 0$ deg, $\theta_B = 30$ deg, and $K_A = K_B = 0.18$ kg m^2/s^2 in the wind tunnel.

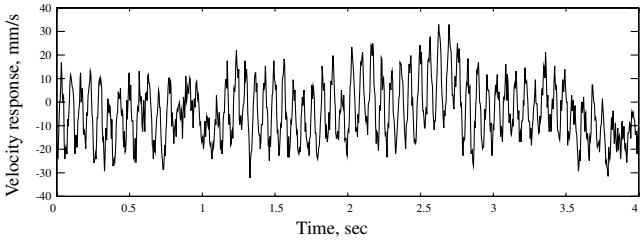

a) U=17.5 m/s

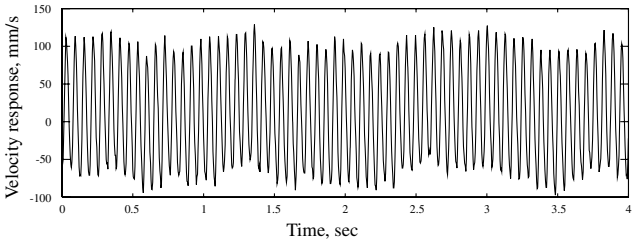

b) U=19.9 m/s

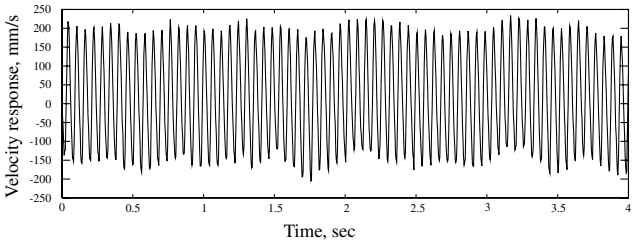

c) U=22.48 m/s

Fig. 19 Measured time histories at several flow velocities for the outboard folding angle, $\theta_C = 0$ deg, $\theta_B = 30$ deg, and $K_A = K_B = 0.18$ kg m^2/s^2.

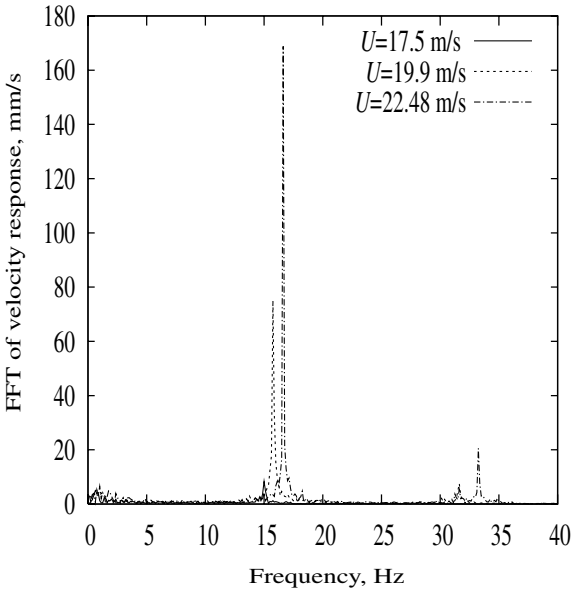

Fig. 20 FFT analysis of the LCO velocity response measured at several flow velocities for the outboard folding angle, $\theta_C = 0$ deg, $\theta_B = 30$ deg, and $K_A = K_B = 0.18$ kg m^2/s^2.

The prediction of the flutter speed from theoretical LCO plots is straightforward because it is simply the speed at which the LCO amplitude tends to zero in the absence of any external disturbances (noise). However, for experimental LCO amplitude plots in the presence of noise, it is far more difficult to make a precise determination of flutter speeds. Instead, a range of flutter speeds whose breadth depends on the level of noise present is usually determined and shown. This issue has been studied for some years, perhaps first being systematically studied in the context of panel flutter [11].

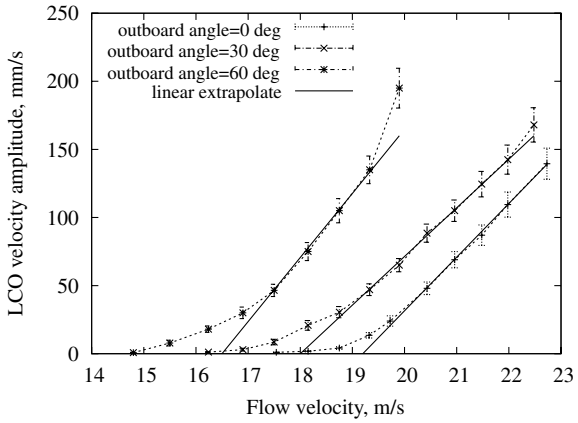

a) LCO velocity amplitude

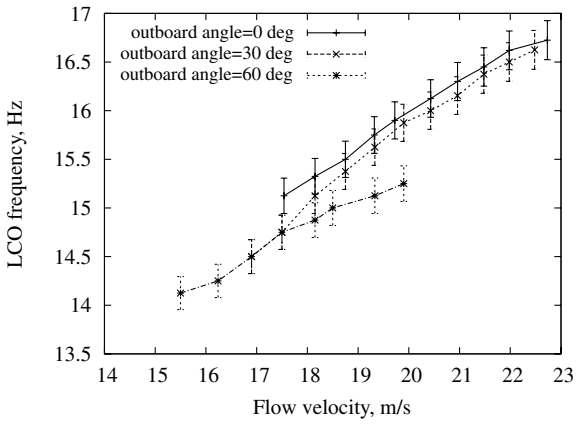

b) LCO frequency

Fig. 21 LCO velocity amplitude and frequency vs flow velocity for several outboard folding angle, θ_C at attachment points for $\theta_B = 30°$ and $K_A = K_B = 0.18$ kg m^2/s^2.

The theoretical and experimental (estimated) critical flutter boundary flow velocities (including an error bar) vs the outboard folding angle are shown in Fig. 15a. Figure 15b shows the corresponding flutter frequency. The correlations between the theory and the experiment are within 10–15% for the flutter boundary and flutter frequency.

V. Conclusions

The structural dynamic behavior and aeroelastic stability of a folding wing aircraft model are studied using a linear plate theory, a component modal analysis, and a three-dimensional time domain vortex lattice aerodynamic model. The results are computed for different inboard and outboard folding angles and for different torsional stiffnesses at the attachment points.

It is found that the natural frequency and the critical flutter velocity of the folding wing system are sensitive to the inboard and outboard torsional stiffnesses when K_A is less than 2.5 and K_B is less than 1.0 kg m^2/s^2. For the present folding wing model, an increase in inboard torsional stiffness leads to improved aeroelastic stability (increasing flutter velocity). However, an increase in outboard torsional stiffness leads to a decrease in aeroelastic stability (decreasing flutter velocity). Thus, an optimum for both the inboard and outboard torsional stiffnesses exists for the aeroelastic design of a folding wing aircraft. It is also noted that the variation of K_A can lead to a hump-type flutter, which will decrease the critical flutter velocity.

The folding structural natural frequency and the critical flutter velocity are also sensitive to the inboard and outboard folding angles. An increase of the inboard folding angle, θ_B, leads to an increase in the flutter velocity when $\theta_B < 60$ deg. However, when the inboard folding angle, θ_B, is larger than 75 deg, the critical flutter velocity drops down. The outboard folding angle, θ_C, also has an optimum flutter velocity at $\theta_C = 0$ deg. An increase in the outboard folding angle leads to a decrease in the flutter velocity.

The theoretical results are compared with the experimental results. The correlations between the theory and the experiment are within 10–15% for both the flutter velocity and frequency.

Acknowledgment

This work was supported under the Air Force Office of Scientific Research grant "Nonlinear High Fidelity Aeroelastic Analysis for Novel Configurations," under the direction of Victor Giurgiutiu.

References

[1] Wlezien, R. W., Horner, G. C., McGowan, A. R., Padula, S. L., Scott, M. A., Silcox, R. H., and Simpson, J. O., "The Aircraft Morphing Program," AIAA 98-1927, April 1998.

[2] Wilson, J. R., "Morphing UAVs Change the Shape of Warfare," *Aerospace America*, Vol. 42, No. 2, Feb. 2004, pp. 28–29.

[3] Dunn, J., Horta, L., Ivanco, T., Piatak, D., Samareh, J., Scott, R., and Wieseman, C., "NASA Contributions to DARPA MAS Program," *Aerospace Flutter and Dynamics Council Meeting*, NASA Langley Research Center, Hampton, VA, May 2004.

[4] Snyder, M., Frank, G., and Sanders, B., "Aeroelastic Analysis of a Morphing Z-Wing Configuration," *Aerospace Flutter and Dynamics Council Meeting*, NASA Langley Research Center, Hampton, VA, May 2004.

[5] Lee, D. H., and Weisshaar, T. A., "Aeroelastic Studies on a Folding Wing Configuration," AIAA 2005-1990, April 2005.

[6] Michael, B. W., and Kamesh, S., "Dynamic Aeroelastic Stability of Morphable Wing Structures," AIAA Paper 2006-2133, May 2006.

[7] Snyder, M., Sanders, B., Eastep, F., and Frank, G., "Sensitivity of Flutter to Fold Orientation and Spring Stiffness of a Simple Folding Wing," *Proceedings of the International Forum on Aeroelasticity and Structural Dynamics 2005*, NASA Langley Research Center, Hampton, VA, June–July 2005.

[8] Dowell, E. H., and Tang, D. M., *Dynamics of Very High Dimensional Systems*, World Scientific Publishing Co., Singapore, 2003, Chap. 10.

[9] Katz, J., and Plotkin, A., *Low-Speed Aerodynamics*, McGraw–Hill, New York, 1991, Chap. 12.

[10] Hall, K. C., "Eigenanalysis of Unsteady Flows About Airfoils, Cascades, and Wings," *AIAA Journal*, Vol. 32, No. 12, 1994, pp. 2426–2432.

[11] Dowell, E. H., *Aeroelasticity of Plates and Shells*, Kluwer Academic, Norwell, MA, 1975.